

PAPER

Measuring individual carbon nanotubes and single graphene sheets using atomic force microscope infrared spectroscopy

To cite this article: Matthew R Rosenberger *et al* 2017 *Nanotechnology* **28** 355707

View the [article online](#) for updates and enhancements.

Related content

- [Improved atomic force microscope infrared spectroscopy for rapid nanometer-scale chemical identification](#)
Hanna Cho, Jonathan R Felts, Min-Feng Yu *et al*.
- [Hyphenated analytical techniques for materials characterisation](#)
Gordon Armstrong and Lekshmi Kailas
- [Topicalreview](#)
H M Pollock and A Hammiche

Recent citations

- [Divergent effect of electric fields on the mechanical property of water-filled carbon nanotubes with an application as a nanoscale trigger](#)
Hongfei Ye *et al*

Measuring individual carbon nanotubes and single graphene sheets using atomic force microscope infrared spectroscopy

Matthew R Rosenberger¹, Michael Cai Wang¹ , Xu Xie²,
John A Rogers^{1,2,3}, SungWoo Nam¹ and William P King^{1,2,4}

¹ Department of Mechanical Science and Engineering, University of Illinois at Urbana-Champaign, 1206 W. Green St., Urbana, IL 61801, United States of America

² Department of Materials Science and Engineering, University of Illinois at Urbana-Champaign, 1304 W. Green St., Urbana, IL 61801, United States of America

³ Department of Materials Science and Engineering, Northwestern University, 2145 Sheridan Road, Evanston, IL 60208, United States of America

E-mail: wpk@illinois.edu

Received 4 May 2017, revised 14 June 2017

Accepted for publication 28 June 2017

Published 1 August 2017



CrossMark

Abstract

Atomic force microscope infrared spectroscopy (AFM-IR) combines the spatial resolution of AFM with the chemical specificity of IR spectroscopy. In AFM-IR, sample absorption of pulsed IR light causes rapid thermomechanical expansion, which excites resonance in an AFM cantilever in contact with the sample. The cantilever resonant amplitude is proportional to the local sample IR absorption coefficient. It is difficult to detect thermomechanical expansion in the smallest samples such as 1D and 2D nanomaterials. In this work, we overcome this limitation and use AFM-IR to measure nanometer-scale IR absorption in individual single walled carbon nanotubes and monolayer graphene. By placing a thin layer of polymer beneath the sample, the AFM-IR signal may be increased by up to two orders of magnitude. The polymer beneath the sample thermally insulates the sample and amplifies thermomechanical expansion. Finite element simulations agree with the measurements and provide a general framework for applying this approach to arbitrary samples, including other 1D and 2D materials and thin biological samples.

Supplementary material for this article is available [online](#)

Keywords: AFM, infrared, nanoIR, CNT, graphene

(Some figures may appear in colour only in the online journal)

Introduction

Infrared (IR) spectroscopy is a widely used technique for measuring the chemical composition of materials [1]. Conventional IR spectroscopy is limited in its resolution to measurements on the order of the wavelength of IR radiation ($\lambda \sim 3\text{--}20 \mu\text{m}$). IR spectroscopy is thus limited in its ability to measure nanometer-scale materials. In comparison, the atomic force microscope (AFM) [2] has excellent spatial

resolution (tip radius $\sim 20 \text{ nm}$), but cannot measure precise information about chemical composition.

Atomic force microscope infrared spectroscopy (AFM-IR) is a powerful tool that combines the spatial resolution of the AFM with the chemical specificity of IR spectroscopy [3, 4]. In AFM-IR, a pulsed infrared laser illuminates the sample, which absorbs some of the incident light. The absorbed light results in heat generation and temperature rise, which in turn results in thermal expansion [3]. An AFM cantilever in contact mode observes the surface expansion, which is proportional to the local sample absorption

⁴ Author to whom any correspondence should be addressed.

coefficient. The major advantage of AFM-IR over other nanometer-scale infrared techniques, such as scanning near-field optical microscopy [5–7], is that the AFM-IR measurement depends directly on IR absorption, which simplifies data interpretation and facilitates the comparison with conventional IR spectroscopy. AFM-IR has been effective for investigations of polymer [8–11] and biological [12] samples, and in some cases metallic [13, 14] and semiconducting [15] samples.

A fundamental limitation of AFM-IR is that the sample must exhibit a thermal expansion that can be measured by AFM. The sample thermal expansion is proportional to thickness, temperature, and thermal expansion coefficient. In practice, samples must be thicker than 15 nm [8], have an attenuation coefficient of at least 400 cm^{-1} (estimated from polymer absorption peaks) [16], and have a coefficient of thermal expansion (CTE) larger than about $14 \times 10^{-6}\text{ K}^{-1}$ (thermal expansion coefficient of gold) [13]. Obviously, not all samples fulfill these criteria. In particular, carbon nanotubes (CNTs) and graphene can have a thickness less than 1 nm [17, 18], and cannot be easily measured in AFM-IR [4]. Extending AFM-IR to the measurement of very thin samples, weakly absorbing samples, and samples with small CTE would provide a valuable tool for studying local infrared absorption in such materials.

In this work, we demonstrate AFM-IR measurements on single walled CNTs and monolayer graphene, with nanometer-scale spatial resolution. The measurements are enabled by a two order of magnitude improvement in AFM-IR sensitivity, which is achieved by placing a thin layer of polymer beneath the sample, which thermally insulates the sample and amplifies thermomechanical expansion. A finite element model of sample thermal and mechanical behavior agrees well with experiments. Using the model, we provide guidelines for the extension of this technique to other samples. The two orders of magnitude improvement in AFM-IR signal demonstrated in this work enables measurement of very thin samples with negligible thermal expansion that were previously not measurable with AFM-IR.

Modeling the AFM-IR system

Figure 1(a) shows the setup for AFM-IR [4]. A pulsed infrared laser passes through a ZnSe prism and reflects off of the prism's top surface, resulting in an evanescent electromagnetic field above the surface which interacts with the sample. The sample absorbs some of the energy from this field, increases in temperature, and expands. Rapid thermomechanical expansion of the sample excites the contacting AFM cantilever into mechanical resonance. The amplitude of the AFM cantilever resonance depends on local thermomechanical expansion which is proportional to the local infrared absorption coefficient.

The key to understanding AFM-IR is that the technique is sensitive to thermomechanical expansion, which is proportional to infrared absorption. The physics of AFM-IR involve four processes: (A) sample absorption of infrared radiation,

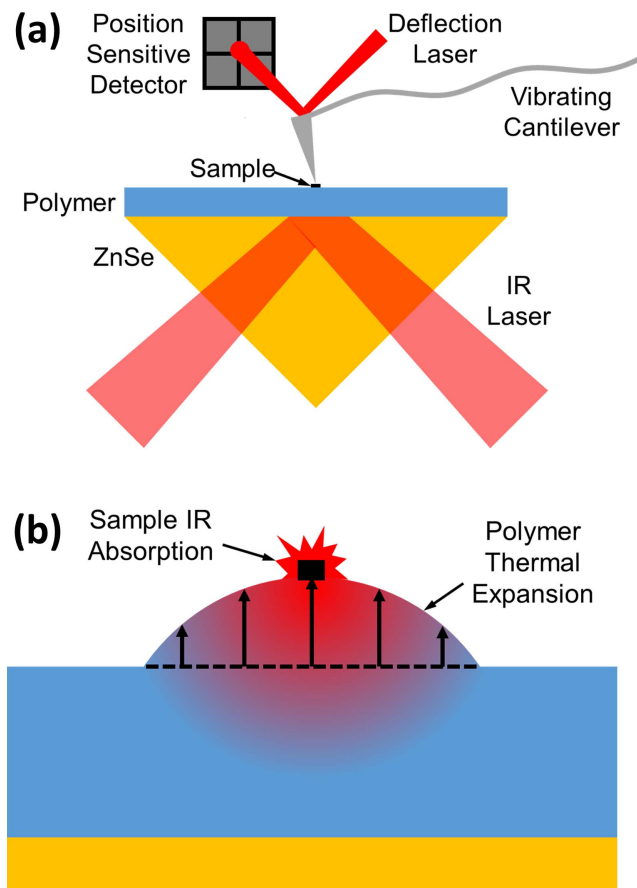


Figure 1. (a) Diagram of atomic force microscope infrared spectroscopy. An infrared laser causes sample heating and associated thermal expansion, which induces measurable cantilever vibration. Typically, the sample is directly on the ZnSe prism. (b) Diagram showing the effect of placing a thin layer of polymer between the sample and ZnSe prism. Sample heating causes a temperature rise and associated thermal expansion in the polymer, which significantly amplifies the cantilever vibration signal.

(B) sample thermal response, (C) sample thermomechanical response, and (D) cantilever response to surface expansion. The desired information from this technique is the local infrared absorption coefficient (process A), which provides chemical specificity. The experimental observable is the cantilever resonance amplitude (process D). The sample thermal and thermomechanical behavior (processes B and C) are intermediate processes that determine the cantilever resonance amplitude for a given absorbed power. A detailed understanding of the thermal and thermomechanical behavior enables the intelligent design of signal amplification.

Placing a thin layer of polymer between the sample and ZnSe prism as shown in figure 1(a) results in signal amplification due to increased thermal insulation and amplified thermomechanical response. Figure 1(b) shows a close-up view of the sample on top of polymer. The sample absorbs IR light, resulting in heat flow into the polymer. As the underlying polymer layer increases in temperature, there is a corresponding thermal expansion, which is measured by AFM.

Table 1. Material properties for finite element model of thermal and thermomechanical behavior.

Material	Thermal conductivity (W m ⁻¹ K ⁻¹)	Density (kg m ⁻³)	Heat capacity (J kg ⁻¹ K ⁻¹)	Thermal expansion coefficient (ppm K ⁻¹)	Poisson's ratio (-/-)	Young's modulus (GPa)
ZnSe	17	5270	339	7.1	0.28	70
Polymer	0.2	1050	1200	100	0.35	3.2
CNT	200	1600	750	5	0.3	500
Air	0.025	1.205	1005			

To investigate the impact of polymer beneath the sample on heat flows and sample deformation, we developed a two-dimensional thermomechanical finite element model. The model geometry consisted of four components: (1) a ZnSe prism substrate, (2) a polymer layer on top of the ZnSe prism, (3) a CNT on top of the polymer layer (approximated as a 2.5 nm diameter circle), and (4) air above the CNT. Table 1 shows the relevant properties for each material. The finite element model included two independent parts: a thermal model to determine the time-dependent temperature and a mechanical model to determine the time-dependent thermomechanical expansion.

The thermal model calculated temperature distributions using the continuum heat equation with constant material properties. A 10 ns heating pulse applied to the CNT simulated heating from a pulsed infrared laser. The boundary condition at the edges of the simulation region was constant temperature. The initial condition was that the entire simulation was at room temperature. Each simulation was 1 microsecond long.

The mechanical model calculated thermomechanical displacements assuming linear elastic behavior with constant material properties. We excluded air from the mechanical model because we assumed that air has a negligible mechanical influence on the other materials. We applied the time dependent temperature solution to the mechanical model to determine the thermomechanical deformation at each time. One boundary condition was that the ZnSe at the simulation boundary was not allowed to move. The other boundary condition was that the top surface of the polymer and CNT were free to move. The initial condition was that the entire simulation was at zero displacement.

The model predicts up to two orders of magnitude increase in thermal expansion when the polymer is beneath the sample. Figure 2(a) shows the predicted effect of polymer thickness on maximum temperature rise and maximum expansion. Increased thermal resistance from the polymer layer leads to increased temperature rise for a given absorbed power. Thermomechanical expansion is proportional to temperature rise, so increased thermal insulation leads to larger thermomechanical expansion. Also, with the polymer beneath the sample, heat must flow through the polymer to reach the prism, which results in polymer temperature rise. Since the polymer has a large thermal expansion coefficient, there is significant thermomechanical expansion from the polymer layer, which amplifies the overall surface expansion.

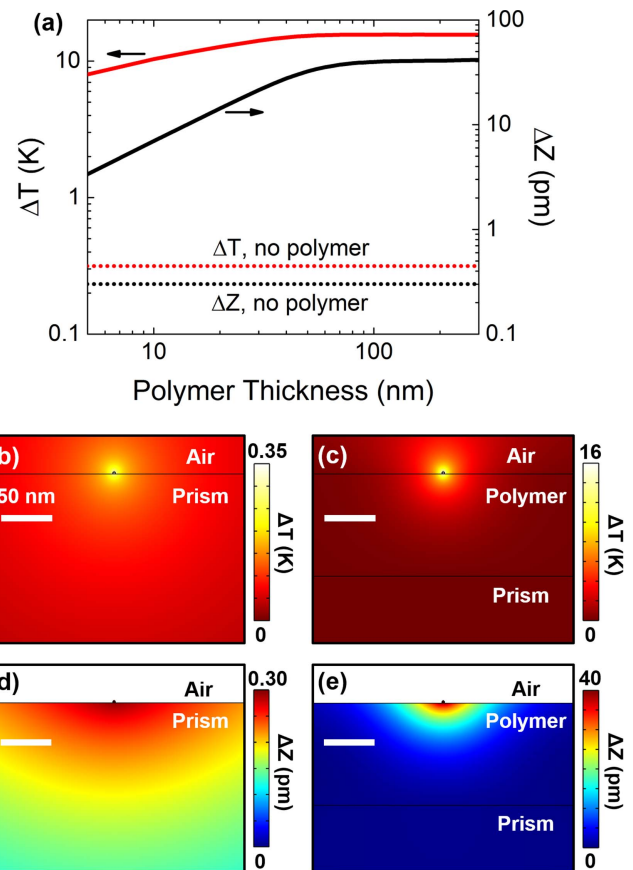


Figure 2. Placing a thin layer of polymer beneath the sample causes a large increase in temperature rise and thermomechanical expansion. (a) Temperature rise (ΔT) and expansion (ΔZ) as a function of polymer thickness beneath the sample. The dotted curves correspond to ΔT and ΔZ with no polymer beneath the sample. (b) and (c) Temperature rise at the end of a 10 ns laser pulse (b) with no polymer and (c) with polymer beneath the sample. (d) and (e) Vertical thermomechanical expansion at the end of a 10 ns laser pulse (d) with no polymer and (e) with polymer beneath the sample.

In fact, the expansion of the polymer enables measurement of samples with negligible thermal expansion.

Figures 2(b) and (c) show that the presence of the polymer beneath the sample increases the temperature rise in the sample for a given absorbed power. Figure 2(b) shows the modeled temperature field at the end of the laser pulse for the sample directly on the ZnSe prism and figure 2(c) shows the temperature field under the same conditions and with 100 nm of polystyrene between the sample and the prism. The

maximum temperature is almost two orders of magnitude larger when the thin layer of polymer is beneath the sample because the polymer is a better thermal insulator than ZnSe as seen in table 1. Also, the thermal penetration depth is much smaller with the polymer layer, with most of the temperature rise concentrated in an approximately circular region around the sample. The nanotube is very small relative to the other dimensions in the system, and behaves similarly to a point heat source, in which the temperature rapidly decreases as a function of distance from the heat source [19]. The maximum temperature does not change significantly for a polymer thickness larger than about 40 nm (figure 2(a)), since beyond this thickness the polymer layer is very large relative to the nanotube diameter. Although the temperature field in the air is similar to the temperature field in the substrate, the quantity of heat flow through the air is small because the thermal conductivity of air is much smaller than the thermal conductivity of the ZnSe prism and the polymer.

Figures 2(d) and (e) show that the polymer beneath the sample amplifies thermomechanical expansion. Figure 2(d) shows the modeled thermomechanical expansion field at the end of the laser pulse for the sample directly on the ZnSe prism and figure 2(e) shows a similar plot with 100 nm of polystyrene between the sample and the prism. The maximum expansion is more than two orders of magnitude larger when the thin layer of polymer is beneath the sample. In both figures 2(d) and (e), the sample contributes negligible thermomechanical expansion. The majority of thermomechanical expansion comes from the polymer that is near the CNT (i.e. near the top surface of the polymer) because this is the region that experiences the largest temperature rise (figure 2(c)). This behavior explains why the maximum expansion does not change significantly above a polymer thickness of about 50 nm (figure 2(a)). Also, due to lateral heat spreading, there is significant thermal expansion from the polymer that is not directly beneath the sample, which has important consequences for spatial resolution, discussed below in more detail.

To compare modeled results with experiments, we developed a finite difference model of cantilever dynamic mechanical behavior which predicted cantilever response to time varying surface expansion [8, 20]. The governing equation for the model was the dynamic Euler–Bernoulli beam equation [20]. The boundary conditions were that the cantilever base was fixed and the displacement of the cantilever free end was equal to the surface displacement calculated from the finite element model. With these boundary conditions, we used our time domain finite difference code to determine the cantilever deflection as a function of time at each location along the surface. The deflection signal in AFM is proportional to the cantilever slope where the deflection laser reflects from the cantilever (the deflection laser was at the free end for this work, as shown in figure 1(a)). To approximate the deflection signal, we calculated the average slope of the last 30 μm (approximate laser spot size) at the cantilever free end. Finally, we calculated the Fourier transform of the deflection signal as a function of time in order to

determine the cantilever resonance amplitude at each location along the surface.

Experimental methods

Sample preparation

AFM-IR samples consisted of a ZnSe prism, spin-coated polymer, and CNTs or graphene transferred on top of the polymer. First, ZnSe prisms were cleaned with acetone and isopropanol, and then dried with nitrogen. Then the prism was secured in a plastic chuck and mounted on a spinner. Spin-casting polymer/solvent solutions on the top surface of the ZnSe prism produced polymer thin films. We achieved polystyrene thicknesses ranging from 15–150 nm by spin casting polystyrene/toluene solutions with different polystyrene concentrations (0.5–2% wt) and spin speeds (1000–3000 rpm). We also achieved approximately 100 nm films using PMMA 495 A2 from Microchem. The polymer films were baked on a hotplate at 100 °C for at least five minutes after spinning.

CNT and graphene samples were produced by chemical vapor deposition and transferred onto the polymer coated ZnSe prisms. CNTs were transferred onto the polymer thin films using a polyvinyl alcohol (PVA) transfer technique. Briefly, we coated the CNTs (on quartz substrate) with a PVA/water solution of ~10% wt and dried the PVA film on a hotplate at 60 °C. We gently pressed thermal release tape onto the PVA film. Using tweezers, we quickly removed the thermal release tape, which removed the PVA film and CNTs. The thermal release tape/PVA/CNT was placed onto the polymer coated ZnSe prism. We heated the sample on a hotplate at 110 °C to remove the thermal release tape. Finally, we used DI water to remove the PVA. Graphene transfer was accomplished by etching the growth substrate, which caused graphene to float on the surface of water. Then the graphene was scooped out of the water onto the polymer coated ZnSe prism.

AFM-IR Experiments

We performed AFM-IR experiments on an Anasys Instruments NanoIR system. We used triangular silicon nitride cantilevers for the measurements (Bruker DNP-10, cantilever C). The experimental absorption signal was the amplitude of the cantilever resonance mode near 1450 kHz. Maps of infrared absorption were obtained with an average of 16 laser pulses per pixel. For CNT measurements, we used 100% laser power. For graphene measurements, we used less than 50% laser power because 100% laser power caused excessive graphene heating, which led to polymer melting. To assess spatial resolution for CNTs, we measured linescans perpendicular to the CNTs. For the spatial resolution measurements, we used an average of 32 laser pulses per pixel. We averaged at least four linescans for each spatial resolution measurement.

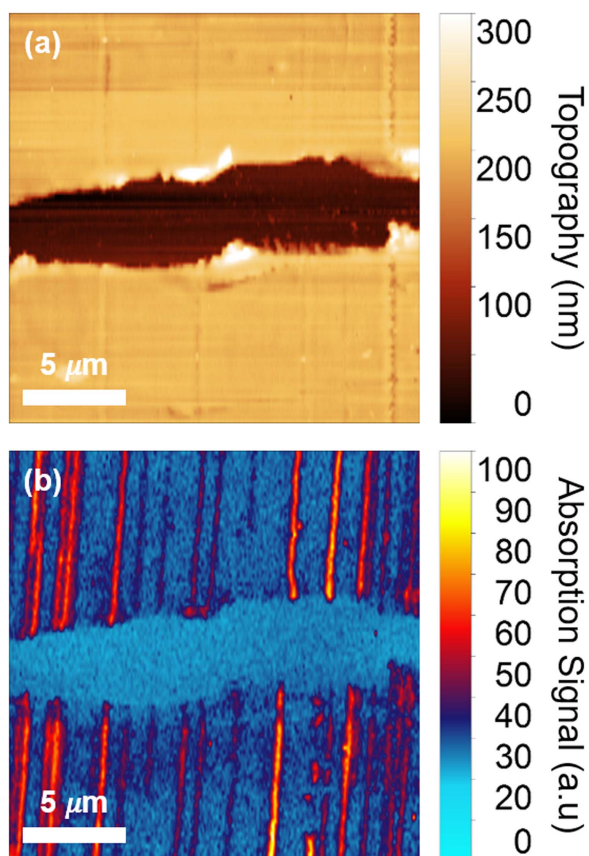


Figure 3. Measurements of carbon nanotube infrared absorption. (a) Topography of sample consisting of CNTs transferred on top of polystyrene with one strip scratched away before CNT transfer. (b) Expansion signal corresponding to absorption at 4000 cm^{-1} .

Results and discussion

Figure 3 shows measurements of individual CNT infrared absorption, which demonstrates the signal enhancement of placing polymer beneath the sample in AFM-IR. Figure 3(a) shows a $20\text{ }\mu\text{m} \times 20\text{ }\mu\text{m}$ topography image of the sample. The sample consists of a 150 nm thick polystyrene layer with one strip scratched away and then an array of aligned CNTs transferred over the top of the polystyrene. Non-contact AFM phase images revealed that CNTs adhered to both the polystyrene and the ZnSe prism (i.e. the region with polystyrene scratched away), as shown in figure S1 in the supplementary information, which is available online at stacks.iop.org/NANO/28/355707/mmedia. Figure 3(b) shows local infrared absorption with the laser tuned to 4000 cm^{-1} ($2.5\text{ }\mu\text{m}$). The CNTs are clearly distinguishable and have different levels of signal, which we hypothesize is due to different infrared absorption based on metallic versus semiconducting character [21, 22]. The regions between CNTs on polystyrene have an absorption signal that corresponds to polystyrene. The region with no polystyrene has no absorption signal, even where the CNTs are present, which indicates that the polystyrene layer amplifies the signal from CNTs. We found that the absorption signal both on and off of CNTs was linear with respect to power, indicating that the sample and cantilever responses are linear. This is not surprising because the

equations governing heat transfer and mechanics in these experiments are linear if the material properties are constant. As a result, the cantilever response on the CNT (due to absorption from the CNT and polymer) is a linear combination of the cantilever response to polymer absorption and the cantilever response to CNT absorption. We can estimate the CNT absorption signal by subtracting the signal on the CNT from the signal off of the CNT.

The polymer layer absorbs some of the incident light, which is a source of uncertainty in the measurement. In general, low polymer absorption (i.e. low background signal) is desired, and, if possible, the polymer layer should be selected such that it does not exhibit strong IR resonance near those of interest in the sample being analyzed. Depending on the wavelength range of interest, different polymers will provide lower background signal. For example, Teflon has no strong resonances from $1500\text{--}4000\text{ cm}^{-1}$, which makes it an ideal candidate for measuring samples in that range. In some cases, the IR light absorbed by the polymer can be advantageous, if used to probe electric field enhancement in plasmonic and antenna-like structures, as has been demonstrated for gold microresonators [14]. The key difference of our technique compared with previous work is that the polymer is beneath the sample rather than on top of the sample. The benefit of placing the polymer beneath the antenna is that the polymer will amplify the AFM-IR signal due to antenna heating. This enables measurement of both antenna field enhancement (laser tuned to polymer resonance) and antenna self-heating (laser tuned off of polymer resonance) on the same antenna.

Figure 4 shows quantitative agreement between experiments and modeling for polystyrene thickness below 80 nm and qualitative agreement above 80 nm . Figure 4(a) shows normalized absorption signal linescans for a CNT on three different polystyrene thicknesses: 15 , 80 , and 153 nm . As polystyrene thickness increases, the width of the response increases due to lateral heat spreading in the polymer film and the associated thermal expansion from polystyrene that is not directly beneath the CNT. For 153 nm of polystyrene, the shape of the experimental and modeled linescans are slightly different. One possible explanation is that the physical properties of the polymer film depend on the thickness. Figure 4(b) shows the effect of polystyrene thickness on the full width at half maximum (FWHM) for experiments and the model. The error bars on the experimental data points represent the standard deviation from measurements on at least three different CNTs. The branched black curves represent the model results for polymer thermal conductivity between $0.1\text{--}0.4\text{ W m}^{-1}\text{ K}^{-1}$. Below 125 nm , FWHM is independent of thermal conductivity. Above 125 nm , FWHM is larger for higher thermal conductivity. Employing FWHM as a metric of spatial resolution, the experimental spatial resolution for 15 nm of polystyrene is $33 \pm 3\text{ nm}$. FWHM for 80 nm of polystyrene is $103 \pm 11\text{ nm}$. The model and experiments both exhibit the same trend over the entire range of polystyrene thickness: FWHM increases as polystyrene thickness increases. The general agreement between the model and experiments over the range of polystyrene

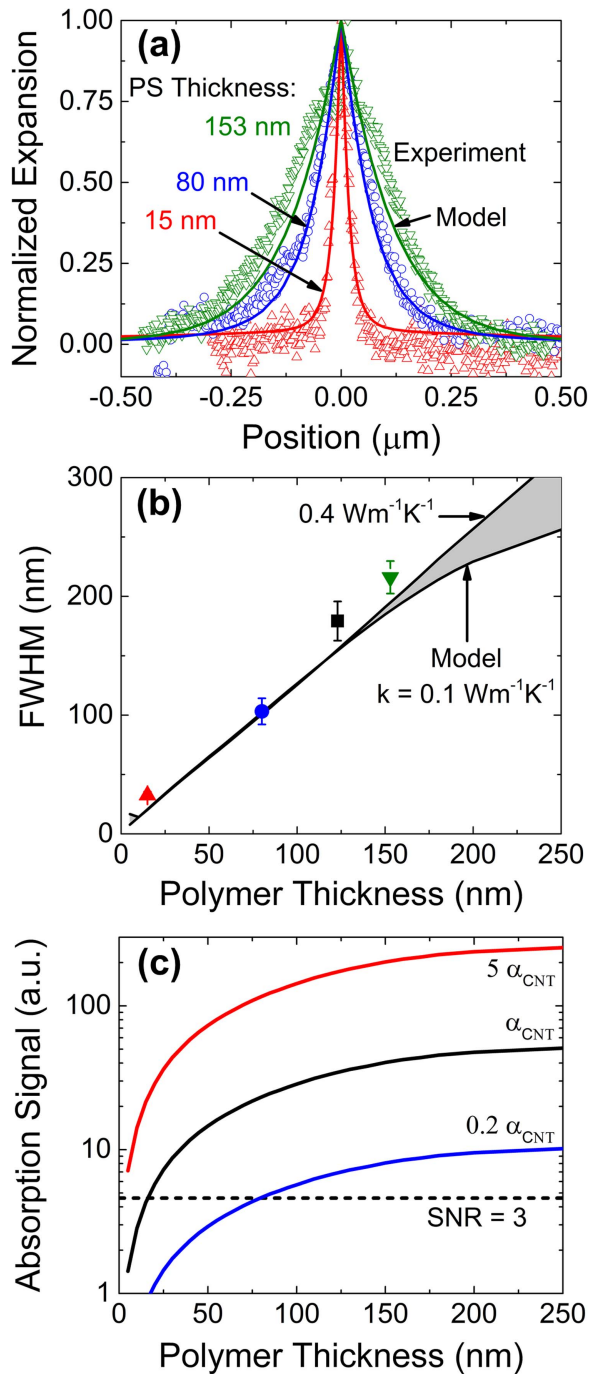


Figure 4. Effect of polymer thickness on spatial resolution and signal enhancement. (a) Comparison of experimental (points) and modeled (solid lines) linescans of a CNT on top of three different polystyrene (PS) thicknesses. (b) Full width at half maximum (FWHM) as a function of polystyrene thickness for experiments (points) and model (solid lines). The branched black curves represent the range of FWHM for polymer thermal conductivity ranging from $0.1\text{--}0.4 \text{ W m}^{-1}\text{K}^{-1}$. (c) Absorption signal as a function of polystyrene thickness for three different values of CNT absorptivity. The dotted curve represents experimental signal to noise ratio (SNR) of 3.

thickness from 15–150 nm indicates that the model captures the physics of this technique.

Figure 4(c) shows the modeled expansion signal as a function of polystyrene thickness for three different values of

absorptivity. Expansion signal increases approximately linearly as a function of polystyrene thickness below 125 nm of polystyrene. Above 125 nm of polystyrene, the expansion signal increases by a small amount until the expansion signal plateaus around 250 nm of polystyrene. The explanation for this plateau is that the thickness becomes larger than the thermal penetration depth from the sample into the polymer. Adding an additional polymer beyond the thermal penetration depth results in no additional expansion because this additional polymer does not heat up. Practically, figure 4(c) indicates that no more than 150 nm of polystyrene should be used with this technique. Using a thickness larger than 150 nm will likely yield worse results because the background signal will increase, but the signal enhancement will remain approximately the same.

Figures 4(b) and (c) provide a guideline for the application of this technique to arbitrary samples. There is an important tradeoff between signal enhancement and spatial resolution. While signal increases approximately linearly with thickness up to 125 nm, FWHM also increases linearly in this range. When choosing a polymer thickness, there are two important factors: required spatial resolution and expected absorptivity, α . We estimate that the absorption coefficient of a metallic CNT is $5 \times 10^4 \text{ cm}^{-1}$ [22]. Assuming a nanotube thickness of 2 nm, Beer's Law [23] predicts the absorptivity of a metallic CNT is 1%. The solid black line in figure 4(c) corresponds to the absorptivity of a strongly absorbing CNT (assumed to be metallic) measured in this work, which serves as the reference point for using figure 4(c) with arbitrary samples. The dotted horizontal line in figure 4(c) represents a signal to noise ratio (SNR) of 3 for the measurement of a metallic CNT where the signal corresponds to the average cantilever amplitude over 32 laser pulses and the noise corresponds to the standard deviation of cantilever amplitude for repeated linescans. $\text{SNR} = 3$ (dashed black curve) intersects α_{CNT} (solid black curve) at 16 nm polystyrene thickness. Therefore, for samples with absorptivity greater than or equal to α_{CNT} , 16 nm of polystyrene should provide $\text{SNR} \geq 3$. For samples with absorptivity smaller than α_{CNT} , more than 16 nm of polystyrene is needed to achieve $\text{SNR} = 3$. The solid colored curves correspond to different absorptivity relative to α_{CNT} . The absorption signal is proportional to absorptivity, so the colored curves represent a linear scaling of the black curve. The intersection of the dashed $\text{SNR} = 3$ line with a given solid curve indicates the required polystyrene thickness to achieve $\text{SNR} = 3$ for a sample with the corresponding absorptivity.

In addition to the thickness of polymer, the type of polymer is an important consideration when applying this technique. There are three criteria to consider when choosing a polymer to place beneath the sample: (1) CTE, (2) thermal conductivity, and (3) wavelength of strong IR resonances. The signal enhancement is directly proportional to CTE, so the polymer with the largest CTE will work best. In the range of $0.1\text{--}0.4 \text{ W m}^{-1}\text{K}^{-1}$ (range for typical polymers), signal enhancement is proportional to the thermal resistivity (inverse of thermal conductivity). Therefore, polymers with lower thermal conductivity will provide better signal enhancement.

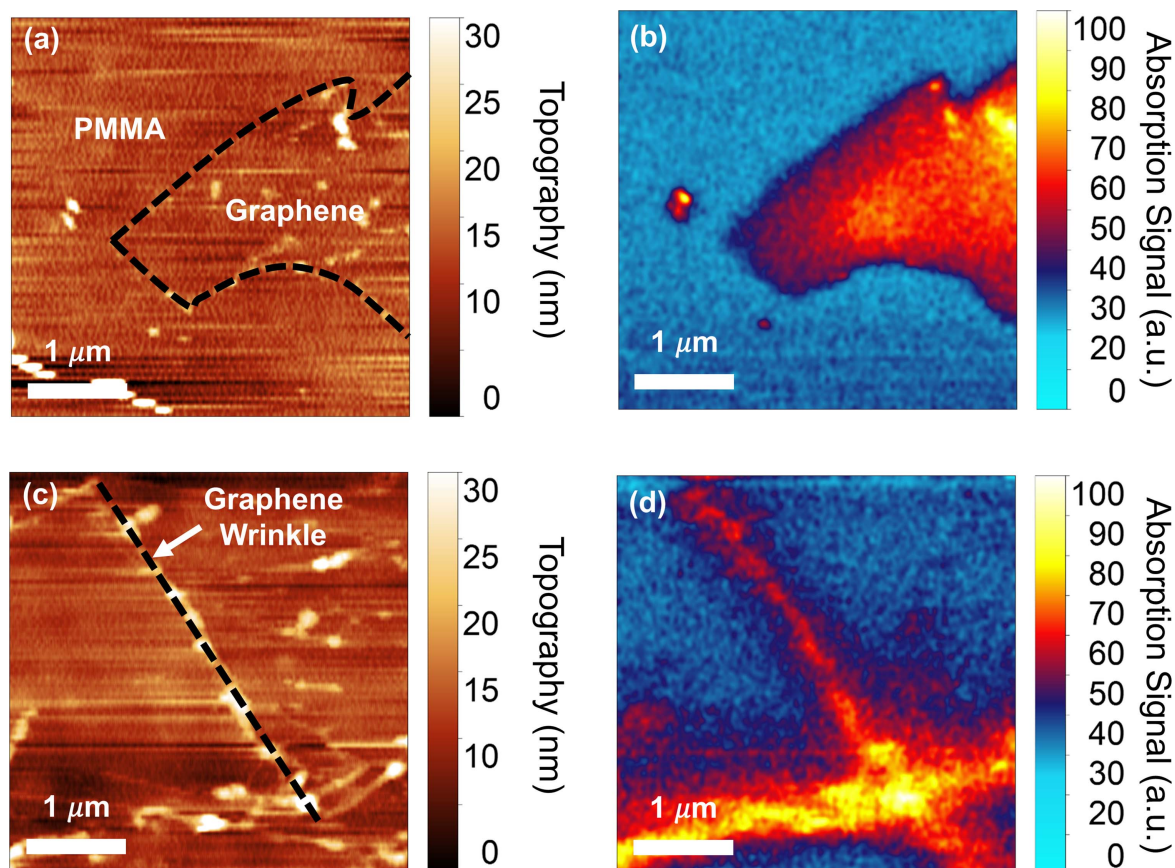


Figure 5. (a) Topography and (b) infrared absorption signal at 4000 cm^{-1} of a graphene sample on top of PMMA. (c) Topography and (d) infrared absorption signal at 2850 cm^{-1} of a graphene wrinkle on top of PMMA. PMMA thickness was 106 nm for both sets of images.

Finally, for the purpose of enhancing signal from the sample, it is best to choose a polymer with small IR absorption in the wavelength range of interest in order to reduce the background signal from the polymer.

Figure 5 shows a measurement of local infrared absorption of graphene with the polymer beneath the sample, which demonstrates the extension of this technique to 2D materials. Figure 5(a) shows topography of a graphene sample transferred onto a 106 nm thick PMMA layer. The dashed black line shows the border of the graphene region. Figure 5(b) shows the absorption signal at 4000 cm^{-1} corresponding to the topography in figure 5(a). This image shows that the measurement is sensitive to graphene absorption. Figure 5(c) shows topography of a graphene wrinkle from a different region of the same sample. Figure 5(d) shows the corresponding absorption signal at 2850 cm^{-1} . The graphene wrinkle shows a clear absorption signal and provides a useful feature for assessing the spatial resolution of the technique when applied to a 2D material.

For a 2D material, lateral heat spreading in both the polymer and the 2D material affect spatial resolution. To assess the spatial resolution, figure 6(a) shows the experimental absorption signal profile perpendicular to the graphene wrinkle labeled in figure 5(c). The experimental FWHM for the graphene wrinkle on 106 nm of PMMA is 380 nm. Figure 6(a) also shows the corresponding model

predictions assuming three different graphene thermal conductivities: 75, 25, and $0\text{ W m}^{-1}\text{ K}^{-1}$. The 2D material model was identical to the 1D material (CNT) model, except with the addition of a 1 nm thick thermally conductive sheet of material on top of the polymer, which approximated the 2D material. Heat spreading in the polymer is similar for 1D and 2D materials. As graphene thermal conductivity increases, the width of the peak increases due to lateral heat spreading in the graphene. The experiment agrees well with the model for $75\text{ W m}^{-1}\text{ K}^{-1}$ graphene thermal conductivity, indicating that the graphene thermal conductivity is $75\text{ W m}^{-1}\text{ K}^{-1}$.

Figures 6(b) and (c) provide a guideline for using this technique with 2D materials when lateral heat spreading in the material may be important. Figure 6(b) shows FWHM as a function of polymer thickness for different 2D material thermal conductivities. The spatial resolution of this technique will be best for materials with low thermal conductivity. Graphene has high thermal conductivity, so this technique should provide better spatial resolution for other 2D materials than for graphene. Figure 6(c) shows absorption signal as a function of polymer thickness for different 2D material thermal conductivity. The signal enhancement from this technique will be highest for lower thermal conductivity materials because less lateral heat spreading leads to larger local temperature rise and larger local thermomechanical expansion.

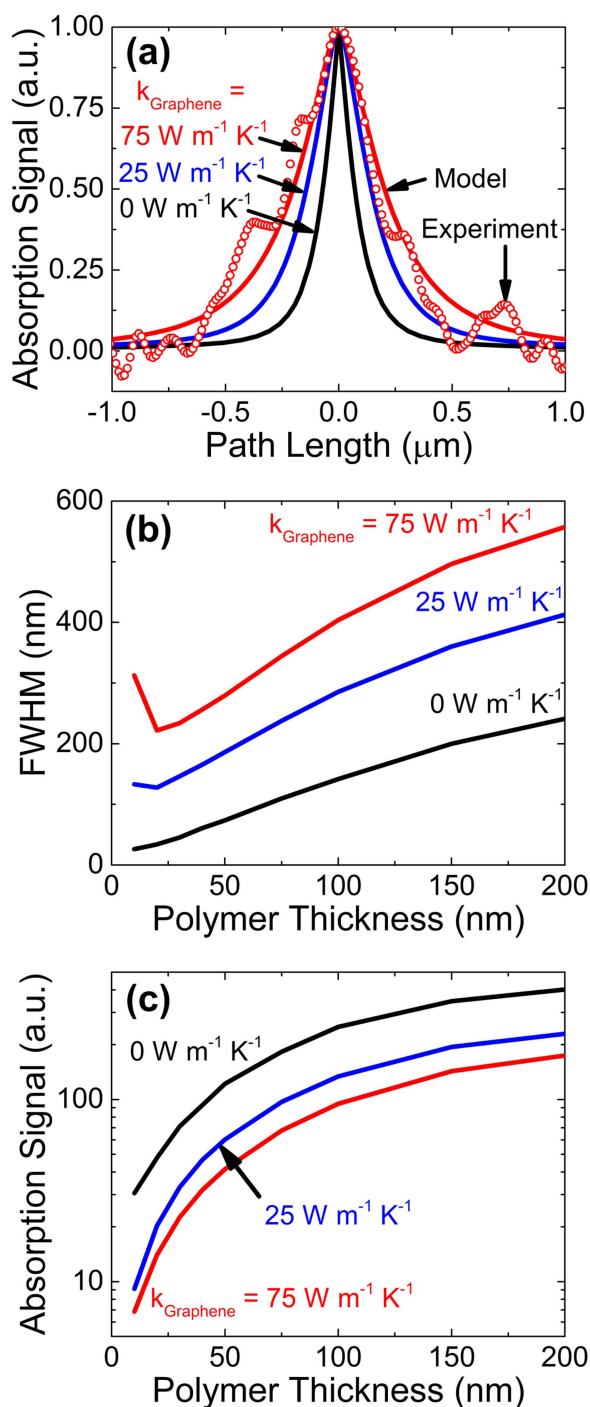


Figure 6. (a) Comparison of experimental (points) and modeled (solid lines) profiles perpendicular to a graphene wrinkle on top of polymer. Three different model curves are shown which represent graphene thermal conductivity of 75, 25, and $0 \text{ W m}^{-1} \text{ K}^{-1}$. (b) Modeled full width at half maximum (FWHM) as a function of polymer thickness for each graphene thermal conductivity. (c) Modeled absorption signal as a function of polymer thickness for each graphene thermal conductivity.

Conclusion

This work presents measurements of infrared absorption in single walled CNTs and monolayer graphene with spatial resolution as good as 33 nm using AFM-IR. These

measurements require an increase in the sensitivity of AFM-IR, which we accomplish by placing a thin polymer layer ($<150 \text{ nm}$) beneath the sample. The polymer layer amplifies the thermomechanical expansion signal by up to two orders of magnitude. A finite element model describing heat diffusion and thermomechanical behavior agrees well with experiments. Signal enhancement and FWHM are approximately linear up to 125 nm of polymer, so thicker polymer layers will improve signal at the cost of decreased spatial resolution. The drastic signal enhancement from the polymer beneath the sample enables AFM-IR measurements of materials with small or negligible thermal expansion, such as ultrathin biological samples and 1D and 2D materials.

Acknowledgement

This work was supported by the Department of Energy Office of Science Graduate Fellowship Program (DOE SCGF), made possible in part by the American Recovery and Reinvestment Act of 2009, administered by ORISE-ORAU under contract no. DE-AC05-06OR23100.

ORCID

Michael Cai Wang  <https://orcid.org/0000-0003-3300-852X>

References

- [1] Stuart B 2000 Infrared spectroscopy *Kirk-Othmer Encyclopedia of Chemical Technology* (New York: Wiley)
- [2] Binnig G, Quate C F and Gerber C 1986 Atomic force microscope *Phys. Rev. Lett.* **56** 930–3
- [3] Dazzi A, Glotin F and Carminati R 2010 Theory of infrared nanospectroscopy by photothermal induced resonance *J. Appl. Phys.* **107** 124519
- [4] Dazzi A, Prazeres R, Glotin E and Ortega J M 2005 Local infrared microspectroscopy with subwavelength spatial resolution with an atomic force microscope tip used as a photothermal sensor *Opt. Lett.* **30** 2388–90
- [5] Heinzelmann H and Pohl D W 1994 Scanning near-field optical microscopy *Appl. Phys. A* **59** 89–101
- [6] Amenabar I *et al* 2013 Structural analysis and mapping of individual protein complexes by infrared nanospectroscopy *Nat. Commun.* **4** 2890
- [7] Chen J N *et al* 2012 Optical nano-imaging of gate-tunable graphene plasmons *Nature* **487** 77–81
- [8] Felts J R, Cho H N, Yu M F, Bergman L A, Vakakis A F and King W P 2013 Atomic force microscope infrared spectroscopy on 15 nm scale polymer nanostructures *Rev. Sci. Instrum.* **84** 023709
- [9] Van Eerdenbrugh B, Lo M, Kjoller K, Marcott C and Taylor L S 2012 Nanoscale mid-infrared evaluation of the miscibility behavior of blends of dextran or maltodextrin with poly(vinylpyrrolidone) *Mol. Pharmaceutics* **9** 1459–69
- [10] Dazzi A, Prater C B, Hu Q C, Chase D B, Rabolt J F and Marcott C 2012 AFM-IR: combining atomic force microscopy and infrared spectroscopy for nanoscale chemical characterization *Appl. Spectrosc.* **66** 1365–84

- [11] Felts J R, Kjoller K, Lo M, Prater C B and King W P Sep 2012 Nanometer-scale infrared spectroscopy of heterogeneous polymer nanostructures fabricated by tip-based nanofabrication *ACS Nano* **6** 8015–21
- [12] Policar C, Waern J B, Plamont M A, Clede S, Mayet C, Prazeres R, Ortega J M, Vessieres A and Dazzi A 2011 Subcellular IR imaging of a metal-carbonyl moiety using photothermally induced resonance *Angew. Chem., Int. Ed.* **50** 860–4
- [13] Katzenmeyer A M, Chae J, Kasica R, Holland G, Lahiri B and Centrone A 2014 Nanoscale imaging and spectroscopy of plasmonic modes with the PTIR technique *Adv. Opt. Mater.* **2** 718–22
- [14] Lahiri B, Holland G, Aksyuk V and Centrone A 2013 Nanoscale imaging of plasmonic hot spots and dark modes with the photothermal-induced resonance technique *Nano Lett.* **13** 3218–24
- [15] Felts J R, Law S, Roberts C M, Podolskiy V, Wasserman D M and King W P 2013 Near-field infrared absorption of plasmonic semiconductor microparticles studied using atomic force microscope infrared spectroscopy *Appl. Phys. Lett.* **102** 152110
- [16] Zolotarev V M, Volchek B Z and Vlasova E N 2006 Optical constants of industrial polymers in the IR region *Opt. Spectrosc.* **101** 716–23
- [17] Xiao J L *et al* 2009 Alignment controlled growth of single-walled carbon nanotubes on quartz substrates *Nano Lett.* **9** 4311–9
- [18] Novoselov K S, Geim A K, Morozov S V, Jiang D, Zhang Y, Dubonos S V, Grigorieva I V and Firsov A A 2004 Electric field effect in atomically thin carbon films *Science* **306** 666–9
- [19] Carslaw H S and Jaeger J C 1986 *Conduction of Heat in Solids* (Oxford: Clarendon)
- [20] Turner J A, Hirsekorn S, Rabe U and Arnold W 1997 High-frequency response of atomic-force microscope cantilevers *J. Appl. Phys.* **82** 966–79
- [21] Du F *et al* 2014 Laser-induced nanoscale thermocapillary flow for purification of aligned arrays of single-walled carbon nanotubes *ACS Nano* **8** 12641–9
- [22] Ichida M, Saito S, Nakano T, Feng Y, Miyata Y, Yanagi K, Kataura H and Ando H 2011 Absorption spectra of high purity metallic and semiconducting single-walled carbon nanotube thin films in a wide energy region *Solid State Commun.* **151** 1696–9
- [23] Mills A F 1992 *Heat Transfer* (Homewood, IL: Irwin)